ChemistrySelect

Research Article
doi.org/10.1002/slct.202402303

Chemistry Europe
European Chemical Societies Publishing

www.chemistryselect.org

The Cu/La@TiO_x Composite: A Sustainable and Efficient Photocatalyst for *N*-benzylation Reaction Under Visible Light

Mohammad Reza Razavi,[a] Zahra Toozandehjani,[a] Yahya Absalan,*[b] Mostafa Gholizadeh,*[a] and Reza Samavati[c]

In this study, a green and sustainable approach using visible light photocatalysis was employed for synthesizing *N*-benzyl aniline derivatives to create C—N bonds. A TiO_2 photocatalyst doped with copper and lanthanum was prepared to reduce the band gap and increase surface area. $Ti_xCu_yO_z$ and $Ti_xCu_yLa_mO_z$ nano-photocatalysts were designed efficiently for organic reactions. Characterization techniques included TEM, FE-SEM, XRD, EDX, FT-IR, BET, BJH, UV–vis, ICP-MS, CV, PL, and TPC. Using visible light as a renewable source, these photocatalysts showed high activity and recyclability up to five times, with $Ti_xCu_yLa_mO_z$ displaying superior performance due to increased lanthanide content.

1. Introduction

The construction of valuable C—X bonds is essential in synthesizing pharmaceuticals and natural products.[1,2] Those compounds contain C—N bonds like amines are among the most common characteristics of bioactive compounds which are often used as essential intermediates in material synthesis.[3–6] Many drugs and bioactive molecules contain at least one C—N bond, such as DNA, RNA, and so forth.[7] According the great importance and remarkable biological activity of amines, especially their pharmacophore properties in most biological compounds, secondary amines have attracted much attention in synthesizing pharmaceutical compounds. Therefore, the development of new and efficient methods for the synthesis of amines has become an active area of research.[8–13] as a way to synthesize *N*-benzylated, *N*-alylated, and *N*-alkylated amines, traditionally, KOH and t-BuOK bases, sodium amide, and CsOH are used.[14–17] Methanol and dimethyl carbonate have also been used as alkylating agents.[18–20] However, all the stated cases require harsh reaction conditions.[21,22] It is remarkable that *n*-substituted amines are conventionally synthesized by direct alkylation but this process has significant limitations, such as excessive alkylation, the toxic nature of some alkyl halides, and low selectivity.[23,24] In order to overcome this deficiency transition metal-catalyzed cross-coupling reactions have been developed for the synthesis of secondary type and third amines such as the Ullmann cross-coupling reaction, Buchwald amination, hydroamination, and hydrogen borrowing method.[25–29] However high temperatures, high catalyst loading, expensive catalysts, and long reaction times are usually required in these strategies.[30,31] Recently heterogeneous catalysts have been widely investigated in organic synthesis due to their high selectivity, excellent thermal stability, and easy recycling. Among the heterogeneous catalysts, metal oxides such as SiO_2, Al_2O_3, and so forth. TiO_2 is a powerful photocatalyst in organic transformations as it has advantages such as, increased reaction speed, simplicity of operation, low cost, improved selectivity, and also has been developed for a wide range of different organic reactions.[32–34] Although the formation of C—N bonds by palladium, platinum, and iridium catalysts has been studied, the formation of C—N bonds in the presence of metal oxide catalysts containing Copper nanoparticles has attracted much attention due to its cost-effectiveness, nontoxic nature, and excellent selectivity.[35–39] Recently, along with thermal organic syntheses, dual photoredox, and transition metal catalysts have been shown as one of the most potent and effective methods for C—N bond formation and other cross-coupling reactions.[40–43] In addition, dual catalytic systems use a unique feature called photocatalytic hydrogen atom transfer (HAT)[51] and excitedstate single electron transfer (SET), which can create high efficiency and excellent selectivity at ambient temperature.[43–50] Expensive photocatalysts such as palladium,[52] ruthenium,[53] and photosensitizer compounds[54,55] are necessary at this stage. Alkyl and aryl radicals are successfully created in the photoreaction.[56–60] It is a unique mechanism for developing economical catalytic systems for making C(sp^3)—N bonds in the presence of stabilized free radicals and activated X—H bonds on the catalyst surface. Copper as a metal with high abundance is a good choice for capturing aryl radicals and activating other substrates containing heteroatoms.[61,62] The wide application of photocatalysis makes them into an integral part of the synthetic chemist's toolbox. The visible light of photocatalysis is associated with several advantages that have led to various applications in the synthesis of

[a] *M. R. Razavi, Z. Toozandehjani, M. Gholizadeh*
Department of Chemistry, Faculty of Sciences, Ferdowsi University of Mashhad, Mashhad, Iran
E-mail: m_gholizadeh@um.ac.ir

[b] *Y. Absalan*
Department of Chemistry, Georgia University, Athens, Georgia 30602, USA
E-mail: yahya.absalan@uga.edu

[c] *R. Samavati*
Department of Organic chemistry, RUDN University, 6 Miklukho-Maklaya St., Moscow 117198, Russia

Supporting information for this article is available on the WWW under https://doi.org/10.1002/10.1002/slct.202402303

heterocyclic compounds as well as in the field of medicinal chemistry.[63,64] Although C—N bond formation has been done by various photocatalysts such as TiO_2 nanoparticles,[65] PANI-g-C_3N_4-TiO_2 nanocomposite,[66] nickel-amine complex, and so forth.[67] The photocatalytic synthesis of *N*-benzylated derivatives of aniline by titania-doped has been rarely reported. In this work, $Ti_xCu_yO_z$ and $Ti_xCu_yLa_mO_z$ composites were hydrothermally synthesized. Then they were used as photocatalysts to synthesize *N*-benzyl aniline derivatives under visible light. Also, the changes in band gap and active surface area in the presence of copper[68] and lanthanum[69] and the synergistic effects to improve organic reaction efficiency were investigated.

2. Experiment

2.1. Material Characterization

The XRD patterns were obtained by a GNR Explorer Advance diffractometer using 1.541 Å(Cu-Kα) radiation. BET and Langmuir analyses were carried out to measure the surface activity of the nanoparticles using capillary condensation of nitrogen at 77 K on a micrometric Belsorp-mini II. The Barrett–Joyner–Halenda method (BJH) was used to estimate the mesoporosity and pore size distribution function. Microscopic images, including FESEM, and TEM, were conducted by scanning electron microscopy (LEO 1430VP LEO 912AB) utilizing Ethanol as the disperser. The diffuse reflection/transmittance spectroscopy (DRS/DTS) was obtained from Avantes (Avaspec-2048-TEC). The FT-IR spectra were recorded on pressed KBr pellets using an AVATAR 370 FT-IR spectrometer (Therma Nicolet spectrometer, USA) at room temperature in the range of 4000–400 cm^{-1} and a resolution of 4 cm^{-1}. Cyclic voltammetry was performed using an ACM model, GillAC. The concentration of the light-exposed solution was assessed by UV-vis spectroscopy in the range of 200–800 nm, using a Cary-50 scan spectrophotometer (Varian). Photoluminescence analysis of the samples was achieved by Avantes-Avaspec-2048. NMR spectra were obtained by an NMR Bruker Advance spectrometer at 300 (^{1}H-NMR) and 75 (^{13}C-NMR) MHz in Chloroform. The photocatalytic application was carried out by a 300 W Xenon lamp (UV–vis light). The system was cooled down to 20 °C by water circulating. The photocatalytic coupling experiments were conducted in a capped-sealed test tube. All result referred to the isolated products after purification by plate chromatography.

2.2. Materials and Reagents

The main precursor chloride metal salts of titanium, copper, lanthanide, and NH_3 were acquired from Merck and Sigma-Aldrich with a purity exceeding 99%, without the need for additional purification.

2.3. Synthesis of $Ti_aO_bM_cLa_d$ Nanoparticles

The precursor used in this study was titanium trichloride ($TiCl_3$). A solution of 1 mmol titanium chloride was prepared in 25 mL of water (solution A), while a solution of 0.5 mmol copper chloride salt was prepared in 25 mL of deionized water (solution B). Additionally, a lanthanide solution containing 0.5 mmol of lanthanide chloride salt with the same concentration of transition metal was prepared as solution C. solutions A and B were mixed and stirred for 20 min. For the lanthanide solution, solutions A and C were mixed and stirred for the same duration.

Next, a mixture of 24 mL NH_3 and 15 mL deionized water was added dropwise to the combined solutions and stirred for one day at room temperature. The copper-doped titanium oxide nanoparticles were then synthesized using a hydrothermal process in an autoclave at 113 °C for 24 h (temperature range tested: 100 °C–120 °C). The particles were separated from the solvent by centrifugation, washed with distilled water, and dried at 80 °C for one day. The final step involved calcination of the product at 450 °C with a heating rate of 10 °C/min.

To synthesize TiO_2 without any dopant incorporation, the same process was followed. The photocatalyst synthesis procedure closely followed our previous report.[50]

2.4. Conducting Cyclic Voltammetry Measurements and Studying the Photocurrent Transition of Catalysts (TixCuyOz, TixCuyLamOz)

Cyclic voltammetry was carried out using a three-electrode system, consisting of a working electrode (gold electrode with a diameter of 2 mm), a reference electrode (Ag/AgCl saturated with KCl), and a counter electrode (platinum wire). Prior to the experiment, the environment was purged with N_2 gas for 15 min. The potential range was set from −0.5 V to 1.0 V with a scan rate of 50 mV/s. The IUPAC convention was followed for the analysis, indicating that the flow direction was from right to left. Transient photocurrent analysis was conducted between 0 and 275 sec, showing on and off behavior, using a 100w Xenon lamp at a potential of 0.8 v.

2.5. C—N Cross-Coupling Photocatalytic Reaction

A total of 0.15 mg of a photocatalyst was added to a sealed tube, followed by the addition of 3 mL of a solvent mixture of distilled water and ethanol (1:1). The solution was then stirred for several min. Subsequently, benzyl bromide (1 mmol), aniline (0.8 mmol), and K_2CO_3 (0.65 mmol) were introduced into the sealed tube. The solution was exposed to irradiation under a 300 W Xe lamp for 2.5 h at a light intensity of 0.7 W/cm^2. The progression of the reaction was monitored using thin-layer chromatography (TLC).

Upon completion of the reaction, the photocatalyst was isolated via centrifugation, washed with ethanol (3 × 15 mL), and dried overnight at 70 °C. The reaction mixture was diluted with water and subjected to extraction with dichloromethane (3 × 10 mL). The combined organic phases were dehydrated using anhydrous Na_2SO_4 and then concentrated under reduced pressure at 40 °C. The crude product was further purified through plate chromatography, employing a mixture of *n*-hexane and ethyl acetate (99:1, v/v) as the eluent, resulting in the isolation of pure *N*-benzyl aniline.

Table 1. Chemical–physical features of the samples.

Sample	JCPDS	*d* Value (nm)	Crystallite Size (nm)
TiO_2	96-900-9087	3.51	16.96
$Ti_xCu_yO_z$	96-153-0152	3.53	21.73
$Ti_xCu_yLa_mO_z$	96-101-1240	3.51	13.4
	96-153-0152		

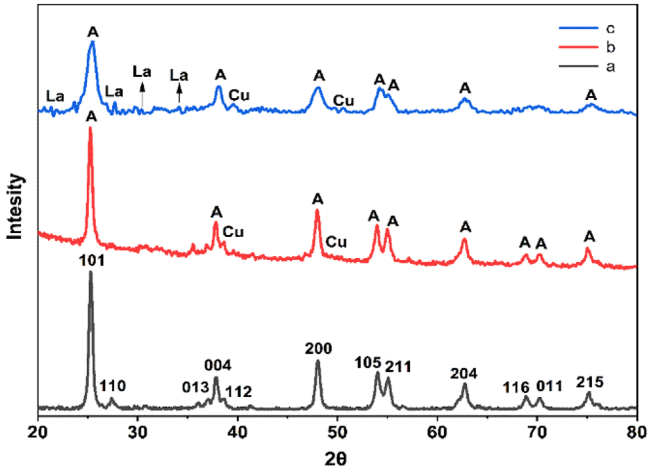

Figure 1. XRD pattern of (a) TiO_2, (b) $Ti_xCu_yO_z$, and (c) $Ti_xCu_yLa_mO_z$.

3. Results and Discussion

3.1. XRD Pattern

XRD patterns were analyzed in the range of 20°–80° ($20° < 2\theta < 80°$) to determine the structure of the nanoparticles. The results indicated that the anatase phase was the predominant phase in the well-crystallite titanium dioxide sample (JCPDS:96–900–9087). The crystallinity type and size of the sample are detailed in Table 1.

Upon doping with copper (Cu), the anatase peaks were mostly retained, with new peaks corresponding to Cu appearing at varying intensities. The d values of the prominent anatase peak exhibited significant changes. The average crystallite size post-doping was similar to that of the pristine TiO_2, determined using the Scherr equation: $D_c = k\lambda\ \beta\cos\theta$. Given the ionic radius of Cu (71pm) compared to Ti (68pm), the incorporation of Cu atoms into the TiO_2 crystallite network could potentially influence the overall crystallite size. The peak related to dopants appeared as a weak peak in the diffraction pattern, and this may be due to the low level of dopant concentration, or it can be assumed that the dopants may have moved in intermediate positions or alternative sites from the crystal network of titanium dioxide.[70] However, according to the XRD pattern obtained after doping by lanthanide (La), the general phase of anatase remains (Figure 1c). The existence of copper in the structure of $Ti_xCu_yLa_mO_z$ was confirmed by observing the peaks related to copper in the XRD pattern of $Ti_xCu_yLa_mO_z$. It can be stated that the crystal size of the sample decreased after doping with lanthanide. The main reasons for the reduction in the crystal size of the sample Based on La doping, it is as follows: (1) lanthanum ions may enter the crystal lattice of titanium dioxide and affect the quality and energy transfer from titania crystal and inhibition growth is adequate, (2) or it may be due to the dissociation of La ions in Grain boundaries prevent the direct contact of seeds and thus reduce the growth of seeds.[71]

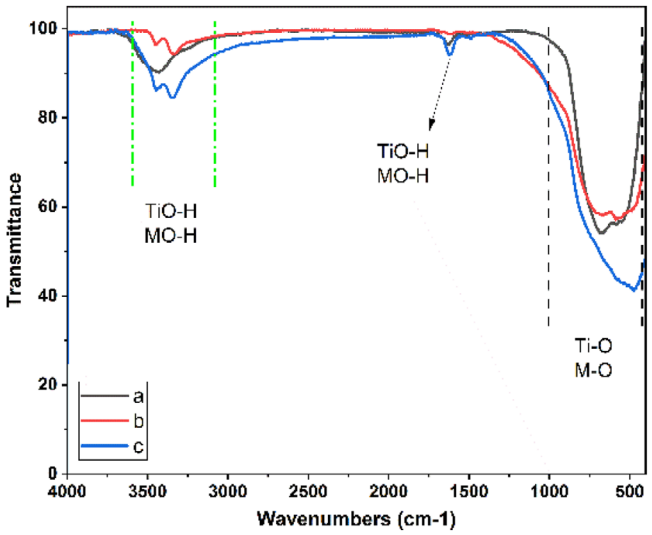

Figure 2. FT-IR spectroscopy of (a) TiO2, (b) TixCuyOz, and (c) TixCuyLamOz.

3.2. FT-IR Spectroscopy

The surface condition of all synthesized nanoparticles was analyzed by using spectrum (FT-IR) in the range of wave number 400–4000 cm^{-1} (Figure 2). The spectrum associated with undoped titania and the absorption peak in the range of 3430–3510 cm^{-1} maybe the result of the stretching vibration of the OH group of absorbed water molecules and hydration on the surface of nanoparticles.[72] However, the intensity of absorption bands in samples doped with copper (Cu) and lanthanide (La) was higher than in undoped TiO_2. Also, the absorption peak at approximately 1620 cm^{-1} (δ(OH)) is related to the absorption of water molecules on the surface of titania and the bending vibration of the TiOH group.[73] The crystal lattice of titania crystallizes as TiO_6 with octahedral molecular symmetry, and the broad peak with good absorption intensity in the region of 500–800 cm^{-1} expresses the stretching vibration of the Ti—O bond in the titania lattice with different types of distortion and crystal defects. In general, the infrared spectrum of titania nanoparticles that are only doped by copper shows less intensity of ν(OH) peaks (Figure 2b).

On the other hand, more intensity is observed for the peaks of the spectrum of titanium dioxide nanoparticles doped with Copper and lanthanide. Therefore, for transition metals doping, the hydrated surface is less, and for double doping of intermediate metal and lanthanum, more hydrated surface is shown.

In general, the absorption peaks from 1000 to 500 cm^{-1} in the spectra of both groups of dopants are related to the stretch-

Research Article
doi.org/10.1002/slct.202402303

Chemistry Europe
European Chemical Societies Publishing

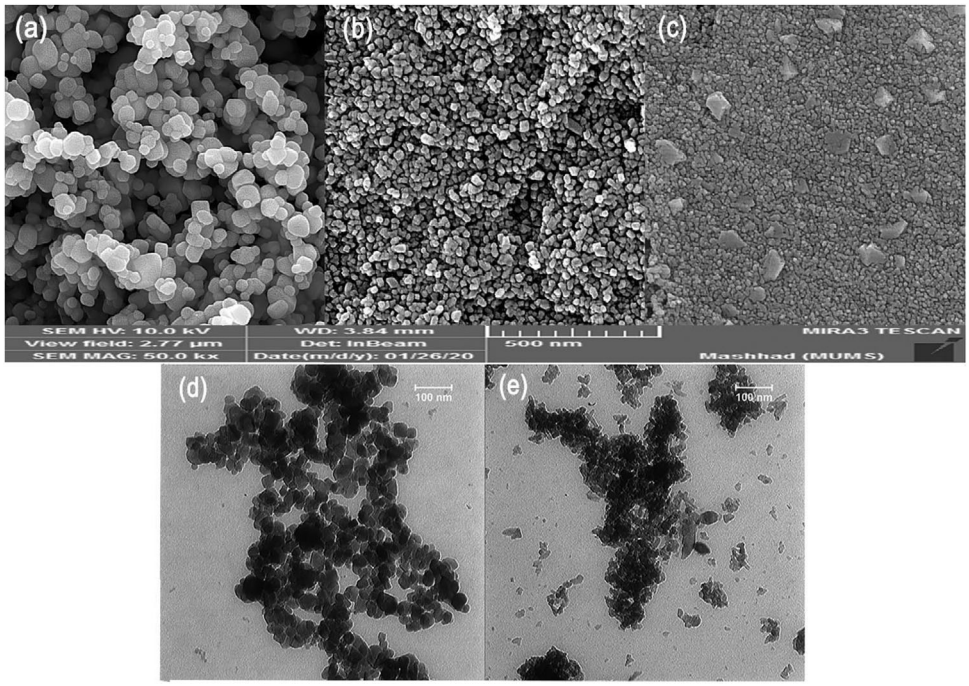

Figure 3. FESEM of (a) TiO_2, (b) $Ti_xCu_yO_z$, and (c) $Ti_xCu_yLa_mO_z$. TEM of (d) $Ti_xCu_yO_z$, and (e) $Ti_xCu_yLa_mO_z$.

ing vibrations of the Ti—O bond and M—O bond. The absorption in the regions as in the spectrum infrared of the synthesized nanoparticles is observed and other absorption peaks related to titania doped by metals are similar to each other. The small peaks at 570 to 500 cm^{-1} indicate the formation of the M—O chemical bond. In addition, the peak created in the region near 550 cm^{-1} in the undoped titania sample, in the presence of Copper and lanthanide, shifts to lower energies, which proves the interaction between different metals and titanium dioxide. In addition, the interaction between Various metals and titanium oxide additional peaks can be observed in the doped samples in the range of 1200 –1350 cm^{-1}, indicating the presence of titanium carbonate on the sample's surface. However, the carbon percentage composition in ICP analysis was reported to be very low.

3.3. FESEM and TEM Analysis

The nanoparticles morphology was analyzed using FE-SEM and TEM techniques (Figure 3). The FE-SEM image revealed that TiO_2 nanoparticles exhibited a bipyramidal shape with significant interparticle space (Figure 3a). Post-doping, the nanoparticles displayed an amorphous structure lacking ordered planes, with reduced interparticle spacing resulting in a denser structure (Figure 3b and c). Different metals were identifiable by varying colors, ranging from white to gray. For $Ti_xCu_yO_z$, the hexagonal shape of TiO_2 was surrounded by smaller, dense spherical particles (Figure 3b). Conversely, lanthanide doping (Figure 3c) resulted in a structure resembling transition metal, with reduced particle size. Further TEM analysis confirmed the presence of various elements (Figure 3e–d). According to calculations of Wolff structure and surface energies in vacuum, the equilibrium shape of the anatase crystal obtained was a slightly truncated bipyramid enclosed by over 94% {101}.[74] The bipyramidal shape of $Ti_xCu_yO_z$ and $Ti_xCu_yLa_mO_z$ particles transformed into a denser form post-doping (indicated by black and gray colors representing impurities and titanium oxide) (Figure 3d and e). Despite this, the samples exhibited good dispersion, confirming the uniformity of particles with appropriate shapes and highlighting the uniqueness of the samples.

3.4. EDX Analysis

Elemental analysis of the samples was performed using EDX analysis to evaluate the elemental distribution and purity of the photocatalysts. According to the results, the elements were uniformly distributed, and all expected elements (Ti, Cu, O, and La) were present in the synthesized photocatalyst $Ti_xCu_yLa_mO_z$ (Figure S1). The absence of even a tiny amount of impurity in this analysis indicates a high purity of the compounds. The EDX results related to the $Ti_xCu_yO_z$ and $Ti_xCu_yLa_mO_z$ photocatalysts are provided in Table S1.

3.5. Inductively Coupled Plasma Mass Spectrometry (ICP)

In order to obtain the total percentage of elements, ICP analysis was used (Table 2). The results in Figure 4 confirm the high purity percentage of the synthesized nanoparticles.

3.6. Surface Analysis

Using BET surface analysis, adsorption-desorption isotherms and pore distribution obtained from the samples are presented in

Table 2. Elemental analysis of the samples.

Sample	Ti (%)	Cu (%)	La (%)	O (%)	Molecular Structure
TiO_2	15	–	–	85	$Ti_{0.34}O_{0.65}$
$Ti_xCu_yO_z$	54	16	–	30	$Ti_{0.63}Cu_{0.24}O_{0.11}$
$Ti_xCu_yLa_mO_z$	59	8	18	15	$Ti_{0.49}Cu_{0.08}La_{0.36}O_{0.05}$

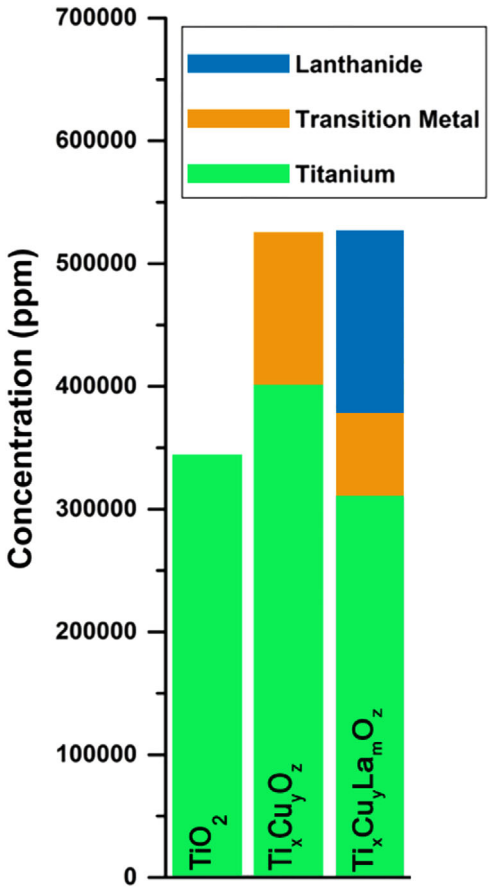

Figure 4. Concentration of different metals in the samples.

(Figure 5). In order to investigate and collect information about the type of porosity, the pore volume has been explored in the P/P_o range of 0–0.99. The surface activity of $Ti_xCu_yO_z$, TiO_2, and $Ti_xCu_yLa_mO_z$ nanoparticles has been investigated by BET analysis (Table 3). Also, the BJH method was used to determine the volume, diameter, and distribution of pores. It is noteworthy that the synthesized nanoparticles have a pseudo-V isotherm, which indicates weak adsorption-desorption. In addition, at higher pressures, hysteresis was observed in the samples. However, the non-rigid accumulation of particles and the conical shape of the pores were confirmed by the H3-type correlation between the shape of the residual ring and the distribution pattern of the samples.[75] At first, it was assumed that lanthanide, due to its larger ionic radius than titanium, does not enter the crystal lattice of titania and is placed on the surface. According to the results of Table 3, it was found that post-doping by lanthanide increased surface activity several times compared to pure titania. It should be mentioned that surface activity is an essential factor

Table 3. Physical–chemical properties of the samples.

BET Analysis

Parameters	TiO_2	$Ti_xCu_yO_z$	$Ti_xCu_yLa_mO_z$
V_m [$cm^3(STP)\ g^{-1}$]	4,1705	6,4803	11,265
$a_{s,BET}$ [m^2g^{-1}]	18,152	28,205	49,029
C	10,938	70,296	68,152
Total pore volume [cm^3g^{-1}]	0,064058	0,1985	0,1954
Mean pore diameter [nm]	14,116	28,158	15,942

BJH Analysis

Parameters	TiO_2	$Ti_xCu_yO_z$	$Ti_xCu_yLa_mO_z$
V_p [$cm^3\ g^{-1}$]	0,066315	0,2	0,1975
$r_{p,peak}$(Area) [nm]	1,22	16,29	6,06
a_p [$m^2\ g^{-1}$]	21,813	35,226	59,399

Table 4. The energy bandgap of the samples.

Sample	Energy Bandgap (eV)	Region
$TiTiO_2$	3.2	
$TiTi_xCu_yO_z$	2.17	
$TiTi_xCu_yLa_mO_z$	2.17	

in photocatalytic reactions. Based on the average pore diameter (in the BJH method), the mesoporosity of $Ti_xCu_yLa_mO_z$ is higher than that of TiO_2.

3.7. UV–vis Absorption

Another critical factor in the performance of photocatalysis is light activity. Therefore, the optical activity of nanoparticles was investigated using reflectance analysis (DRS) in the range of 200–800 nm. Using the formula $-1/[\log_{10}(1/R)]$, where R is the reflectance data DRS reflection was converted to absorption (Table 4 and Figure 6). According to Planck's law ($E = 1/\lambda$), the bandgap energy has an inverse relationship with the wavelength, which means that by reducing the bandgap energy longer wavelengths are absorbed. However, after doping by copper and lanthanide, the band gap energy is reduced compared to pure titania and they can operate in the visible region. For the purpose of calculating the energy of the bandgap, the valuable and accurate Tauk equation was used:

$$\alpha = \alpha_0 \left(h\nu - E_g\right) n/h\nu \quad (1)$$

where α is the absorption coefficient, $h\nu$ shows the photon energy, α_0 and h are constants, E_g denotes the optical bandgap of the material, and n is between 0.5 and 3 (depending on the electronic transition). The plot of $(\alpha h\nu)^2$ versus $h\nu$ can determine the energy bandgap. The $h\nu$ value at the intersection point of the tangent and the X-axis represents the bandgap. According to the results of surface activity and energy gap, copper was more effective compared to lanthanide due to the smaller ionic

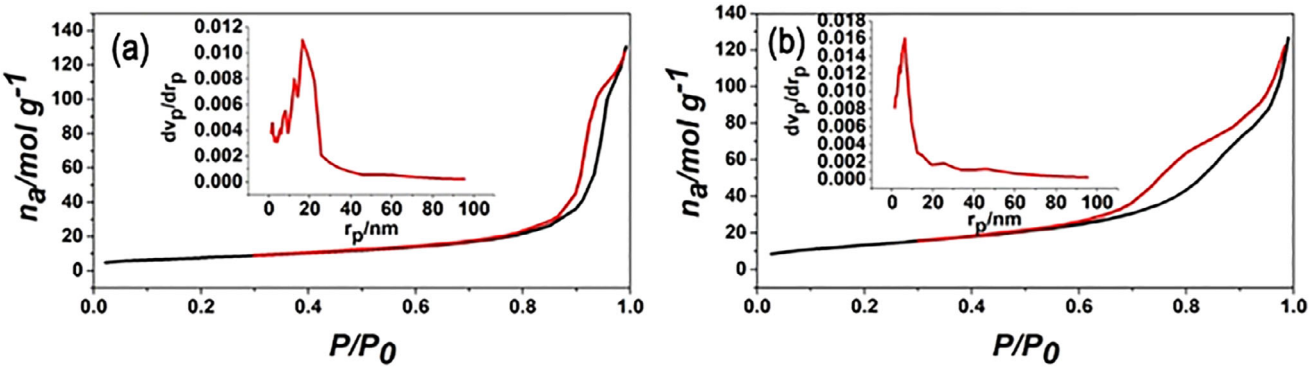

Figure 5. Surface and porosity study of (a) $Ti_xCu_yO_z$, and (b) $Ti_xCu_yLa_mO_z$.

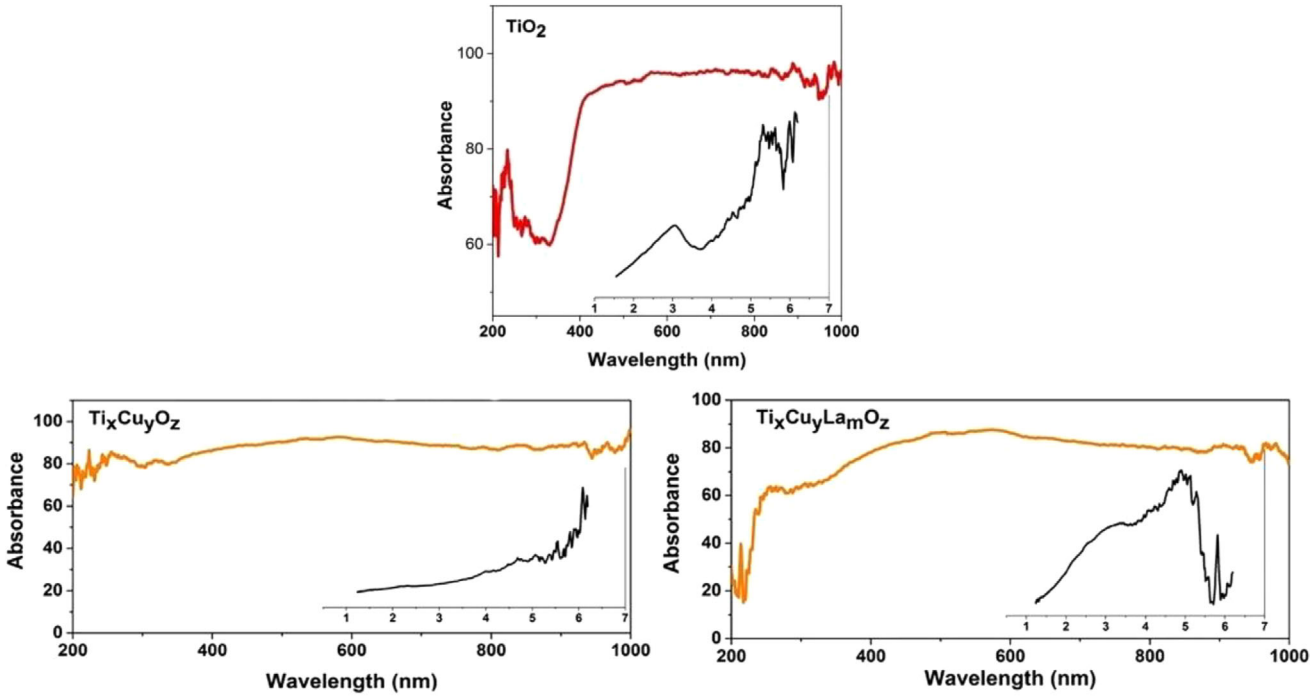

Figure 6. UV–vis spectroscopy of nanoparticles.

radius than titanium. Therefore, it can diffuse in the crystal lattice of titania, which reduces the bandgap and absorbs longer wavelengths. In the case of doping by lanthanide, the bandgap energy is equal to the one doped by copper, which means that lanthanide does not enter the crystal lattice of titania due to its larger radius than titanium and is deposited on the surface. Therefore, it does not have a significant effect on the bandgap.

3.8. Photoluminescence Spectroscopy

In order to further investigate of optical properties of nanoparticles the photoluminescence (PL) emission spectrum was recorded after excitation at 380 nm (Figure 7). The peaks are appearing at 420 nm and 480 nm in the anatase phase of TiO_2 are typical of the rest of the nanoparticles, which indicates the main phase (anatase) of all nanoparticles (Figure 1).

However, the emission peak at 420 nm may be related to the recombination of photogenerated electrons in the valence band.[76] Also, the peak at 480 nm can be associated with the formation of surface defects.[77] Based on the results, TiO_2 nanoparticles have a higher photoluminescence emission intensity than $Ti_xCu_yO_z$ and $Ti_xCu_yLa_mO_z$, which indicates a high rate of recombination in pure TiO_2. The reduction in peak intensity in the case of $Ti_xCu_yO_z$ (red line) may be due to photogenerated charge transfer between copper and titanium in the lattice. However, lanthanide (blue line) has no direct effect on the TiO_2 lattice, while it strongly affects the TiO_2 surface.

3.9. Cyclic Voltammetry Analysis

Cyclic voltammetry was performed to find the LUMO energy (Conduction Band; C.B) of $Ti_xCu_yO_z$ and $Ti_xCu_yLa_mO_z$ (Figure 8).

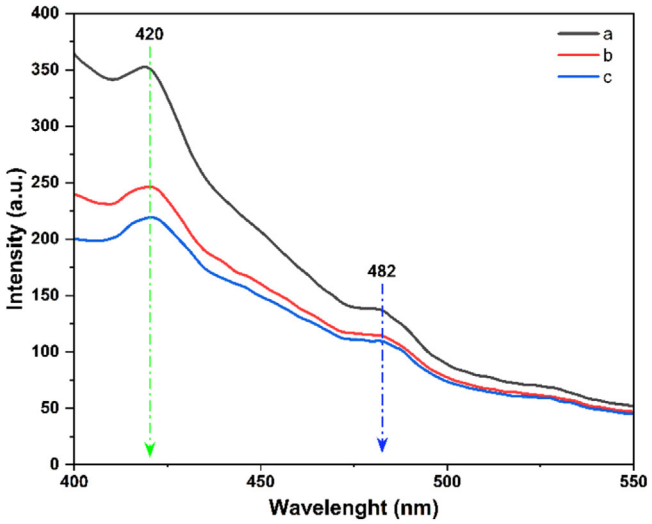

Figure 7. PL spectra of (a) TiO_2 (b) $Ti_xCu_yO_z$ (c) $Ti_xCu_yLa_mO_z$.

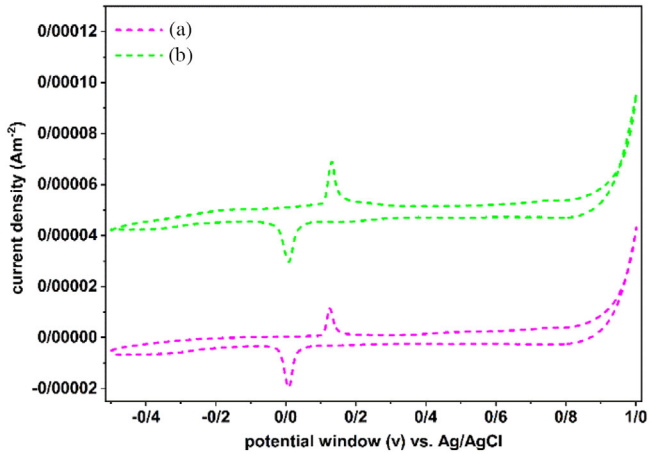

Figure 8. CV analysis of (a) $Ti_xCu_yO_z$ and, (b) $Ti_xCu_yLa_mO_z$.

The catalyst's potential can be converted to surface versus vacuum by $E_{C.B} = -(E_{red} + 4.8)$. Where 4.8 is the correction for the Ag/AgCl pair and NHE.[78] In the case of $Ti_xCu_yO_z$, the $E_{C.B}$ would therefore be −4.84 V versus vacuum. Consequently, the potential of $Ti_xCu_yO_z$ is −0.44 V versus NHE based on $\varphi_{LUMO} = -[E_{C.B} - (-4.4)]$. In the case of $Ti_xCu_yLa_mO_z$, $E_{C.B}$, and $\varphi_{C.B}$ it resulted in −4.83 V and −0.43 V versus NHE, respectively.

3.10. Photocurrent Transient

The photocatalytic performance of the synthesized samples was evaluated by analyzing the Transient photocurrent response. consequently, TiO_2 doped with transition metals and lanthanides showed a higher photocurrent response, indicating the effect of doped elements on the TiO_2 lattice and generating more electron-hole pairs. In Figure 9, the synergistic effect of Cu and La is evident, where the photocatalyst $Ti_xCu_yLa_mO_z$ showed the highest photocurrent response compared to $Ti_xCu_yO_z$ and TiO_2.

4. C—N Cross-Coupling Photocatalytic Reaction

In the field of pharmaceuticals, C—N bonds are often found in the active ingredients of drugs, and their stability and reactivity play a key role in drug design and development.Thus, the photocatalytic cross-coupling reaction under visible light conditions was selected to synthesize of *N*-benzyl aniline derivatives in line with achieving the goals of green chemistry. To find the optimal conditions for the synthesis of *N*-benzyl aniline derivatives by $Ti_xCu_yO_z$ and $Ti_xCu_yLa_mO_z$ photocatalysts, the effect of various parameters such as solvent, light irradiation or non-irradiation and catalyst amount were investigated (Table S2).

For this purpose, a model reaction between aniline (0.8 mmoles, 0.073 mL), benzyl bromide (1 mmole, 0.118 mL) and $Ti_xCu_yO_z$ and $Ti_xCu_yLa_mO_z$ photocatalysts (10 mg) was chosen under room temperature and visible light. In the first step, the model reaction was carried out without of photocatalyst and K_2CO_3 (Table S2, entry 1) and no significant progress was observed. Then, the progress of the model reaction was investigated in the presence of K_2CO_3 without a photocatalyst. However, due to the high yield in the presence of K_2CO_3, subsequent reactions were carried out in the presence of K_2CO_3. In the next step, the model reaction was carried out in the presence of a photocatalyst under visible light irradiation (300 W Xe lamp), which resulted in an increased yield compared to non-irradiation conditions (Table S2, entry 4). Then, the effect of solvent and photocatalyst amount on the progress of the reaction was investigated, and the best results were obtained in ethanol-water solvent (1:1) and 15 mg of photocatalyst (Table S2, entry 11). According to the results, both $Ti_xCu_yO_z$ and $Ti_xCu_yLa_mO_z$ photocatalysts have good efficiency in performing the C—N cross-coupling reaction. Also, $Ti_xCu_yLa_mO_z$ photocatalyst has a higher efficiency compared to $Ti_xCu_yO_z$ in the synthesis of other derivatives (Table S3). Relevant details of the synthesis method and related analyses, including ^{1}H NMR and ^{13}C NMR, are shown in Figures S4-S21.

4.1. Mechanism of Reaction

In order to better understand and accurately determine the mechanism of *N*-benzylation of aniline, a control experiment was performed under optimal conditions. As model reactions, the *N*-benzylation reaction between benzyl bromide and aniline was initially chosen (Scheme 1). The reaction was treated with 2 mmoles of TEMPO (2,2,6,6-tetramethylpiperidin-1-yl) oxyl as an electron-trapping agent. According to the results obtained from the reaction, the product yield (3a) decreased. Additionally, in another investigation, TEA (triethylamine) was used as a hole scavenger in the photochemical reaction. As expected, the yields of the desired products decreased. Moreover, the low yield of product under non-irradiation conditions, as shown in (Table S2), as well as in the presence of TEMPO and TEA indicate that the reaction mechanism likely follows a radical pathway.

In order to understand the process of electron transfer in photocatalysts, the precise positions of the conduction band and

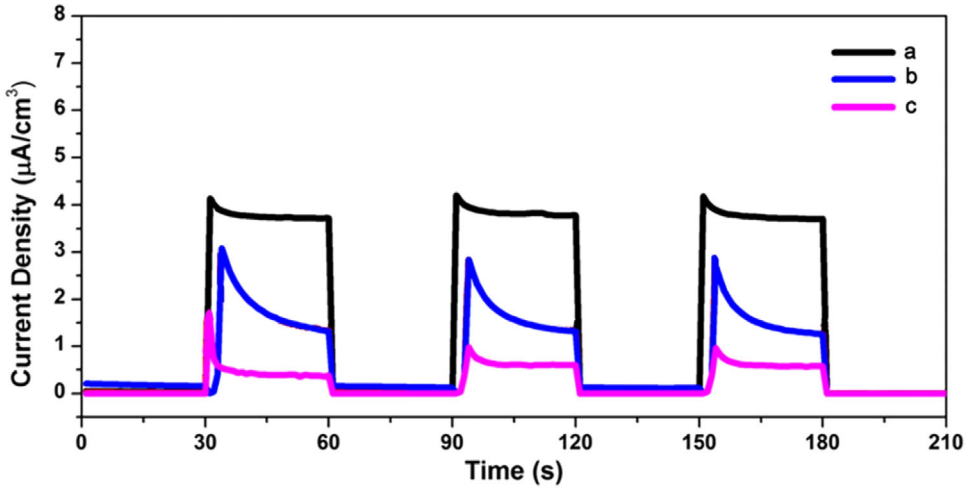

Figure 9. Transient photocurrent response of (a) $Ti_xCu_yLa_mO_z$, and (b) $Ti_xCu_yO_z$, and (c) TiO_2.

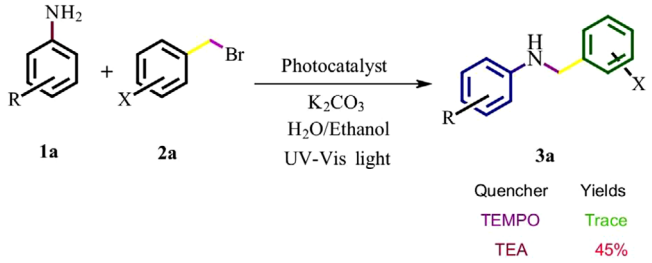

Scheme 1. Control Experiments in *N*-benzylation Reaction.

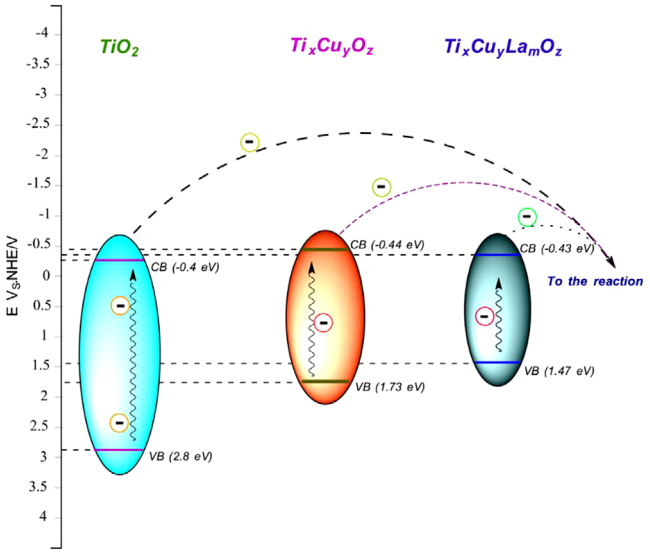

Scheme 2. The CB and VB position in photocatalysts, based on CV and DRS results.

valence band were determined by cyclic voltammetry analysis. In this test, a gold electrode was used as the working electrode, an Ag/AgCl electrode as the reference electrode, and a platinum electrode as the auxiliary electrode. The electrolyte solution used was KCl (0.1 M), and the potential window ranged from 0.5–1 v with a scan rate of 0.05 v/s. Using the cyclic voltammetry plot and the equation $E_{C.B} = -(E_{red} + 4.8)$, the position of the LUMO orbital, which is the position of the conduction band was determined. In this equation, $E_{C.B}$ represents the energy level of the conduction band, and E_{red} is the reduction energy (Figure 8). The number 4.8 is corrected and related to the pair (Ag/AgCl) and the standard hydrogen electrode (NHE).[78] The energy level of the LUMO orbital was calculated using the equation $\varphi_{LUMO} = -[E_{C.B}-(-4.4)]$. The calculated values for $Ti_xCu_yO_z$ and $Ti_xCu_yLa_mO_z$ photocatalysts were –0.44 eV and – 0.43 eV, respectively. Then, in order to determine the energy level of the HOMO orbital, which is the position of the valence band, the values of band gap energy obtained from UV-vis spectroscopy (DRS) were used. The band gap energy values for $Ti_xCu_yO_z$ and $Ti_xCu_yLa_mO_z$ photocatalysts were 2.17 eV and 1.9 eV, respectively. Therefore, the position of the valence band position in the $Ti_xCu_yO_z$ photocatalyst is 1.73 eV, and in the $Ti_xCu_yLa_mO_z$ photocatalyst is 1.47 eV. In order to further investigate the electron transfer process, the positions of the valence band and conduction band of titanium dioxide nanoparticles were also used. Titanium dioxide has a band gap of 3.2 eV, consistent with many published reports on the band gap energy of titanium dioxide. Therefore, in titanium dioxide the position of the valence band is 2.8 eV and the position of the conduction band is −0.4 eV (Scheme 2).[79–83]

Based on the process shown in Scheme 2, at first, the photocatalyst is excited by light absorption and electron-hole pairs are generated in the valence band and migration of electrons from the valence band to the conduction band. According to the electron transfer mechanism in $Ti_xCu_yLa_mO_z$ photocatalyst (Scheme 3), the charge density on the surface of the nanoparticles is high, and. the transferred electrons are sent to the surface of copper and lanthanum nanoparticles, which generate superoxide anion radicals ($O_2^{-\bullet}$) from O_2 present in the air and accelerate the oxidative additional step in coupling with ArX in the corresponding reaction. When the $O_2^{-\bullet}$ interacts with aniline, its proton is absorbed. Consequently, the nucleophile becomes more active for the generation coupling cycle. (Note that K_2CO_3 plays a vital role in forming the nucleophilic intermediate and neutralizing the resulting HX.) Additionally, it is

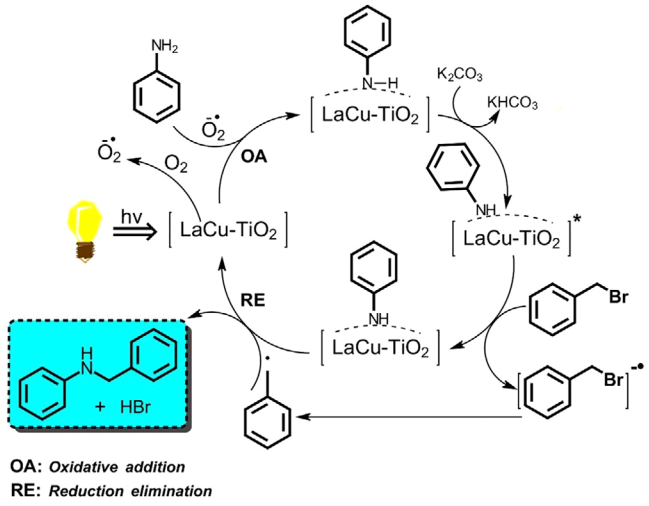

Scheme 3. The proposed mechanism in the synthesis of *N*-benzylaniline.

predicted that a mixture of water and ethanol in the presence of visible light, accelerates the formation of C—N bonds. However, the presence of water by HX solvation, according to Le Chatelier's principle causes the reaction to progress and the presence of ethanol accelerates the mobility of organic species. This prediction has been made based on previous reports.[84–86] Thus, when water and ethanol were used as solvents, the desired product had a higher yield. Therefore, it can be stated that the activated nucleophile is coordinated on the copper surface due to the excellent ability of copper to oxidize/reduce on the surface (oxidative addition step). Consistent irradiation of the light source, the flow of electrons towards the conduction band and the surface of the photocatalyst is continuous, and benzyl bromide, by absorbing electrons from the surface of the photocatalyst, is converted to an anion radical and finally separated into benzyl radical and bromide anion. The formation of benzyl radical through the formation of a small amount of a derivative from bibenzyl was investigated using GC-MS analysis. It was determined that the benzyl radical intermediate is formed and consumed in the reaction cycle (Figure 10a,b). In the end, the interaction of benzyl radical with the intermediate complex formed from aniline and the photocatalyst results in *N*-benzyl aniline (reductive elimination step). The step of adding oxidative on the surface of copper metal in the presence of anionic ligands is accelerated due to the high electron density around the copper metal. In the $Ti_xCu_yLa_mO_z$ photocatalyst, the presence of copper ions reduces the band gap and therefore, increases the absorption range of sunlight. On the other hand, the presence of Lanthanum on the surface of titanium dioxide increases the active surface area and also increases the separation of electron-hole pairs and, as a result, increases the charge density on the surface of the photocatalyst. Additionally, $Ti_xCu_yLa_mO_z$ photocatalyst may act as a Lewis acid in this reaction, activating the amine group and assisting in forming C—N bonds. Therefore, the designed photocatalyst can act as both a photocatalyst and a Lewis acid, resulting in a high yield of the desired product under light conditions.[87–89]

5. Control Experiment: Stability of the Photocatalyst

Catalyst recycling, from both practical and environmental perspectives, is an essential aspect of chemistry and biotechnology. We performed the *N*-benzylation reaction of aniline with benzyl bromide using $Ti_xCu_yLa_mO_z$ as a model reaction to further evaluate its practical applications and stability. After completion of the reaction, the recovered catalyst was washed four times with ethanol and then dried at 80 °C for 12 h. As shown in Figure 11(a), the $Ti_xCu_yLa_mO_z$ catalyst was successfully used in five cycles of experiments. XRD analysis on the catalyst after the fifth reuse demonstrated that the catalyst structure remained unchanged, and under optimal conditions, $Ti_xCu_yLa_mO_z$ is a stable and reusable heterogeneous catalyst Figure 11 shows that the photocatalyst remained robust through five runs, with a slight decrease in yield from 92% to 88% (Figure 11b). Additionally, the stability of the $Ti_xCu_yLa_mO_z$ photocatalyst was confirmed through a leaching test.

6. Leaching Test

The leaching study of the $Ti_xCu_yLa_mO_z$ photocatalyst was conducted using benzyl bromide and 3-chloroaniline as model reactants. Two comparable reactions were set up under identical conditions: one was allowed to proceed for 1 h, while the other continued for an additional 3.5 h after the solid photocatalyst was recovered. The products from both reactions were analyzed as usual. The results indicated that the reaction running for 6 h yielded 48%, whereas the reaction with the recovered photocatalyst produced 50% of the desired product. These findings suggest that the photocatalyst does not leach into the reaction medium and retains its heterogeneity throughout the reaction process.[90–92] Additionally, we compared our results with those reported in the literature (see Table 5).

7. Comparison of Various Types of *N*-benzyl Aniline Synthesis

In Table 5, we have collected information related to different *N*-benzyl aniline synthesis methods, which is interesting. High temperature, prolonged reaction time, and the use of catalysts containing ligands are among the things that were modified and improved in this work.

8. Conclusion

Copper and lanthanum doped titanium dioxide photocatalysts ($Ti_xCu_yO_z$ and $Ti_xCu_yLa_mO_z$) were synthesized and used as photocatalysts under solar light in cross-coupling reactions for the preparation of *N*-benzyl aniline derivatives. The crystalline structure of the synthesized photocatalysts, with pseudo-anatase phases, was confirmed by XRD, FE-SEM, and TEM analyses. The

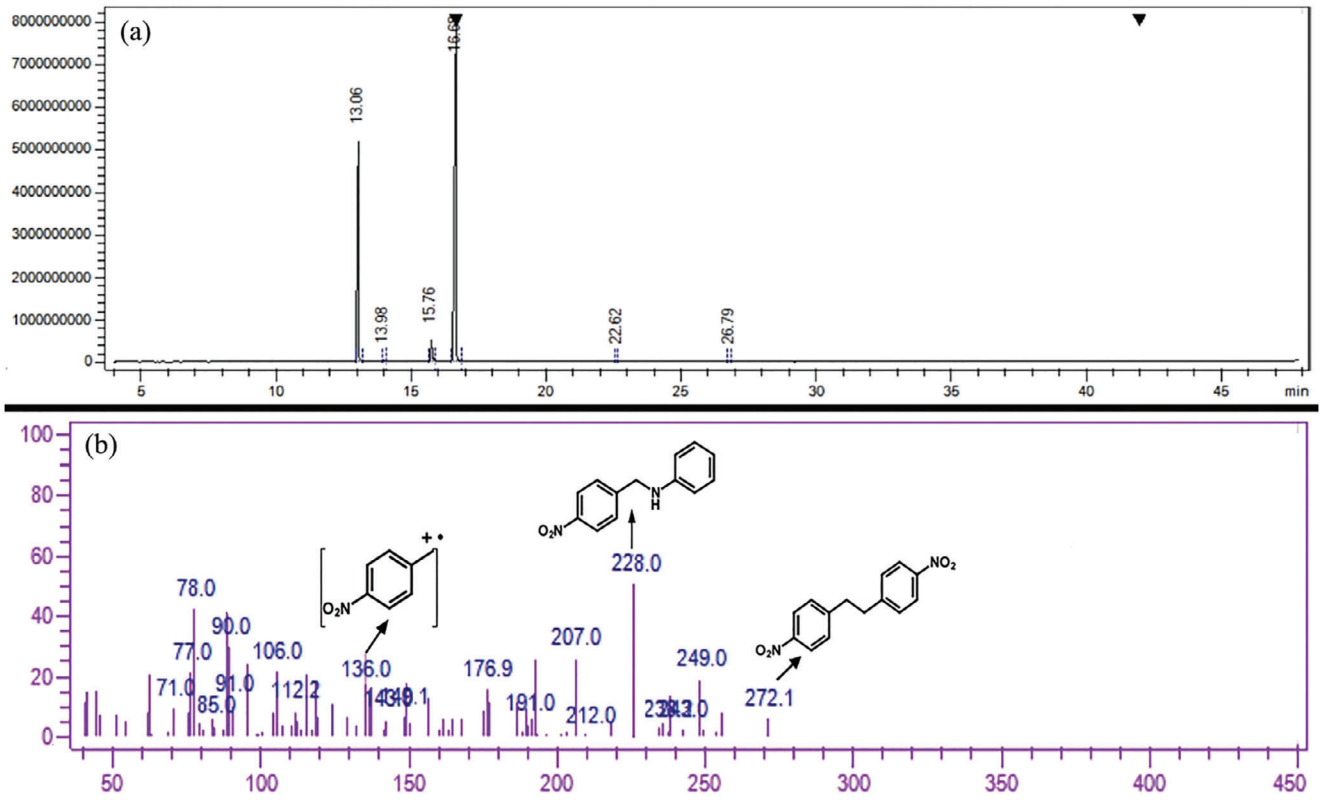

Figure 10. (a) GC-MS Chromatogram, and (b) GC-MS spectrum: Intermediates formed in C—N coupling Reaction.

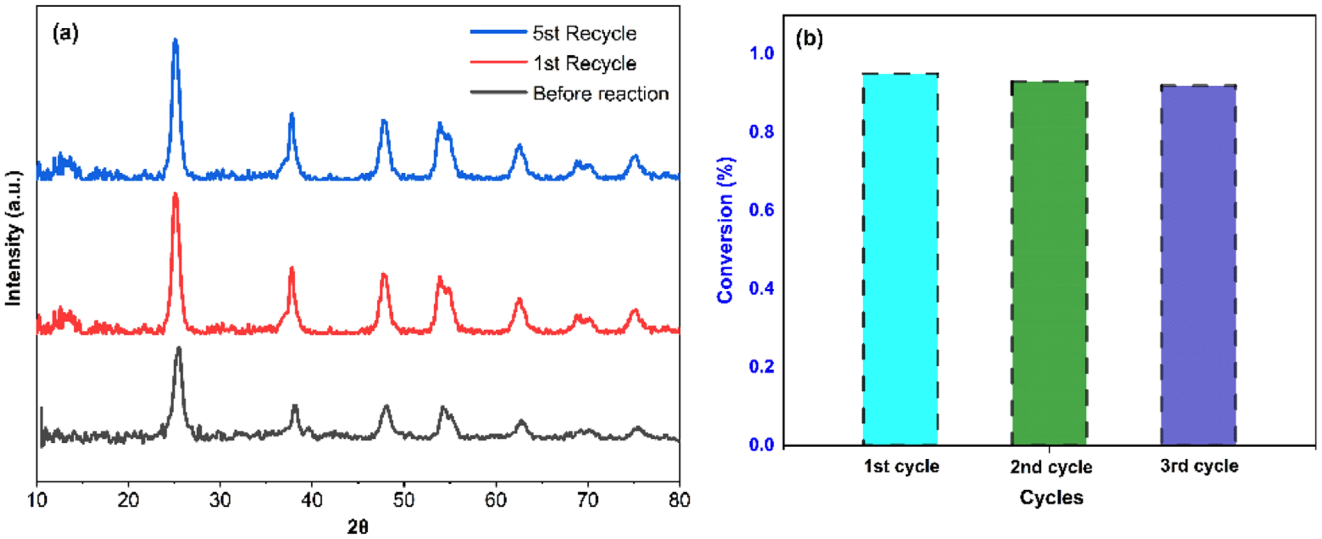

Figure 11. Control Experiment; (a) The XRD patterns of the recycled $Ti_xCu_yLa_mO_z$, (b) Recycling test on $Ti_xCu_yLa_mO_z$.

absence of impurities and the presence of the relevant elements in the prepared composites were also confirmed by EDX and ICP analyses. The photocatalysts showed enhanced visible light activity, lower recombination rate of electron-hole pairs and significantly higher specific surface area than TiO_2, as confirmed by DRS photoluminescence and BET analyses. The $Ti_xCu_yLa_mO_z$ photocatalyst due to its shorter band gap and higher surface activity (due to the deposition of La on the photocatalyst surface, resulting from its larger ionic radius) showed higher efficiency in the C—N bond formation reaction indicating a rational design of this photocatalyst. Furthermore, easy recovery of the synthesized photocatalyst increases the chemical and economic efficiency of this process.

Supporting Information Summary

The authors have cited additional references within the Supporting Information.[87,99–103] The Supporting Information includes detailed explanations of the synthetic methods, materials, and

Table 5. Comparison of various type of *N*-benzyl aniline synthesis.

Reaction	Catalyst	Solvent	Temp (°C)	Time	Yield (%)	Ref.
Reductive amination	$CeCl_3.7H_2O$	EtOH	r.t	8 h	93	[93]
	Silicaphosphoric acid	THF	r.t	15 min	95	[94]
	Ni-Acf@Am-SiO_2@Fe_3O_4	neat	r.t	20 min	98	[95]
	UiO-66-NH-SO_3H	CH_3CN	r.t	5 min	95	[96]
	—	Toluene	150	4 h	96	[97]
Cross-coupling	Cu powder	neat	120	12 h	75	[87]
	SiO_2-Cu_2O	H_2O	30	8 h	95	[88]
	SiO_2-CuI	H_2O	15	4 h	75	[98]
Photocatalytic cross-coupling	$Ti_xCu_yLa_mO_z$	H_2O/EtOH	30	2.5 h	90	This work

experimental procedures utilized in this study. It also covers the characterization techniques employed, such as FT-IR, ^{1}H-NMR, ^{13}C-NMR, EDX, and mapping. Additionally, it features tables outlining the condition optimization for the C—N coupling reactions and the synthesis of *N*-benzylaniline derivatives.

Acknowledgments

We sincerely appreciate the funding provided by Ferdowsi University of Mashhad. We would also like to extend our gratitude to everyone who contributed to this research.

Conflict of Interests

Yahya Absalan reports receiving financial support from the Faculty of Sciences, Ferdowsi University of Mashhad. The other authors declare no conflict of interests.

Data Availability Statement

The data that support the findings of this study are available in the supplementary material of this article.

Keywords: C—N cross-coupling reaction · *N*-benzyl aniline · Photocatalyst · Surface activity

[1] J. F. Hartwig, *Nature* **2008**, *455*, 314–322.
[2] R.-H. Li, Y.-L. Zhao, Q.-K. Shang, Y. Geng, X.-L. Wang, Z.-M. Su, G.-F. Li, W. Guan, *ACS Catal.* **2021**, *11*, 6633–6642.
[3] A. Seayad, *Science* **2002**, *297*, 1676–1678.
[4] S. Suwanprasop, T. Nhujak, S. Roengsumran, A. Petsom, *Ind. Eng. Chem. Res.* **2004**, *43*, 4973–4978.
[5] S. R. Stauffer, J. F. Hartwig, *J. Am. Chem. Soc.* **2003**, *125*, 6977–6985.
[6] H.-J. Böhm, G. Klebe, *Angew Chem. Int. Ed. Engl.* **1996**, *35*, 2588–2614.
[7] E. P. Aparna, D. Mathew, A. Thomas, N. Rakesh, K. S. Devaky, *J. Photochem. Photobiol. A, chem.* **2020**, *399*, 112648–112648.
[8] R. N. Salvatore, C. H. Yoon, K. W. Jung, *Tetrahedron* **2001**, *57*, 7785–7811.
[9] C. Chiappe, D. Pieraccini, *Green Chem.* **2003**, *5*, 193–197.
[10] A. Quintás-Cardama, H. Kantarjian, J. Cortes, *Nat. Rev. Drug Discovery* **2007**, *6*, 834–848.
[11] C. Fischer, B. Koenig, *Beilstein J. Org. Chem.* **2011**, *7*, 59–74.
[12] R. Hili, A. K. Yudin, *Nat. Chem. Biol.* **2006**, *2*, 284–287.
[13] Y. N. Timsina, B. F. Gupton, K. C. Ellis, *ACS Catal.* **2018**, *8*, 5732–5776.
[14] W. C. Guida, D. J. Mathre, *J. Org. Chem.* **1980**, *45*, 3172–3176.
[15] K. Sukata, *Bull. Chem. Soc. Jpn.* **1983**, *56*, 280–284.
[16] Y. Kikugawa, *Synthesis* **1981**, *1981*, 124–125.
[17] S. Hayat, Atta-ur-Rahman, M. I. Choudhary, K. M. Khan, W. Schumann, E. Bayer, *Tetrahedron* **2001**, *57*, 9951–9957.
[18] C. Brielles, J. J. Harnett, E. Doris, *Tetrahedron Lett.* **2001**, *42*, 8301–8302.
[19] S. Narayanan, K. Deshpande, *Appl. Catal. A, General* **1996**, *135*, 125–135.
[20] B. L. Su, D. Barthomeuf, *Appl. Catal. A, General* **1995**, *124*, 73–80.
[21] J. A. O'Meara, N. Gardee, M. Jung, R. N. Ben, T. Durst, *J. Org. Chem.* **1998**, *63*, 3117–3119.
[22] R. N. Salvatore, A. S. Nagle, S. E. Schmidt, K. W. Jung, *Org. Lett.* **1999**, *1*, 1893–1896.
[23] M. H. S. A. Hamid, C. L. Allen, G. W. Lamb, A. C. Maxwell, H. C. Maytum, A. J. A. Watson, J. M. J. Williams, *J. Am. Chem. Soc.* **2009**, *131*, 1766–1774.
[24] C. Bolm, T. Fey, *Chem. Commun.* **1999**, *18*, 1795–1796.
[25] J. Jiao, K. Murakami, K. Itami, *ACS Catal.* **2015**, *6*, 610–633.
[26] F. Khan, M. Dlugosch, X. Liu, M. G. Banwell, *Acc. Chem. Res.* **2018**, *51*, 1784–1795.
[27] P. A. Forero-Cortés, A. M. Haydl, *Org. Process Res. Dev.* **2019**, *23*, 1478–1483.
[28] J. Hannedouche, E. Schulz, *Organometallics* **2018**, *37*, 4313–4326.
[29] T. Irrgang, R. Kempe, *Chem. Rev.* **2019**, *119*, 2524–2549.
[30] R. Shang, L. Liu, *Sci. China: Chem.* **2011**, *54*, 1670–1687.
[31] J. Bariwal, E. Van der Eycken, *Chem. Soc. Rev.* **2013**, *42*, 9283.
[32] L. Liu, A. Corma, *Chem. Rev.* **2018**, *118*, 4981–5079.
[33] Y. Ishino, M. Komatsu, M. Mihara, S. Minakata, *Synlett* **2002**, *2002*, 1526–1528.
[34] L. A. Ghule, A. A. Patil, K. B. Sapnar, S. D. Dhole, K. M. Garadkar, *Environ. Toxicol. Chem.* **2011**, *93*, 623–634.
[35] H. Xu, C. Wolf, *Synfacts* **2009**, *2009*, z893–z907.
[36] J. Jiao, X.-R. Zhang, N.-H. Chang, J. Wang, J.-F. Wei, X.-Y. Shi, Z.-G. Chen, *J. Org. Chem.* **2011**, *76*, 1180–1183.
[37] C. Zou, D. Wu, M. Li, Q. Zeng, F. Xu, Z. Huang, R. Fu, *J. Mater. Chem.* **2010**, *20*, 731–735.
[38] N. T. S. Phan, D. H. Brown, P. Styring, *Green Chem.* **2004**, *6*, 526.
[39] W. Zhou, M. Fan, J. Yin, Y. Jiang, D. Ma, *J. Am. Chem. Soc.* **2015**, *137*, 11942–11945.
[40] M. S. Oderinde, M. Frenette, D. W. Robbins, B. Aquila, J. W. Johannes, *J. Am. Chem. Soc.* **2016**, *138*, 1760–1763.
[41] M. S. Oderinde, N. A. Jones, A. Juneau, M. Frenette, B. Aquila, S. Tentarelli, D. W. Robbins, J. W. Johannes, *Angew. Chem.* **2016**, *55*, 13219–13223.
[42] J. Twilton, C. Le, P. Zhang, M. H. Shaw, R. W. Evans, D. W. C. MacMillan, *Nat. Rev. Chem.* **2017**, 1, https://doi.org/10.1038/s41570-017-0052.
[43] Y. Liang, X. Zhang, D. W. C. MacMillan, *Nature* **2018**, *559*, 83–88.
[44] R. Mao, J. Balon, X. Hu, *Angew. Chem.* **2018**, *130*, 9645–9648.
[45] R. Mao, J. Balon, X. Hu, *Angew. Chem.* **2018**, *57*, 13624–13628.
[46] R. Mao, A. Frey, J. Balon, X. Hu, *Nat. Catal.* **2018**, *1*, 120–126.

[47] J. He, G. Chen, B. Zhang, Y. Li, J.-R. Chen, W.-J. Xiao, F. Liu, C. Li, *Chem* **2020**, *6*, 1149–1159.
[48] V. T. Nguyen, V. D. Nguyen, G. C. Haug, N. T. H. Vuong, H. T. Dang, H. D. Arman, O. V. Larionov, *Angew. Chem.* **2020**, *59*, 7921–7927.
[49] Y. Zheng, X. Shao, V. Ramadoss, L. Tian, Y. Wang, *Synthesis* **2020**, *52*, 1357–1368.
[50] Y. Absalan, M. R. Razavi, M. Gholizadeh, A. Ahmadpour, S. Poursabagh, O. Kovalchukova, *Nano-Struct. Nano-Obj.* **2022**, *30*, 100858–100858.
[51] L. Capaldo, L. L. Quadri, D. Ravelli, *Green Chem.* **2020**, *22*, 3376–3396.
[52] H. Wang, J. Yu, S. Wei, M. Lin, Y. Song, L. Wu, *Chem. Eng. J.* **2022**, *441*, 136020.
[53] E. L. Tyson, Z. L. Niemeyer, T. P. Yoon, *J. Org. Chem.* **2014**, *79*, 1427–1436.
[54] D. P. Hari, B. König, *Org. Lett.* **2011**, *13*, 3852–3855.
[55] J. Yu, L. Zhang, G. Yan, *Adv. Synth. Catal.* **2012**, *354*, 2625–2628.
[56] M.-C. Fu, R. Shang, B. Zhao, B. Wang, Y. Fu, *Science* **2019**, *363*, 1429–1434.
[57] Y.-T. Wang, M.-C. Fu, B. Zhao, R. Shang, Y. Fu, *Chem. Commun.* **2020**, *56*, 2495–2498.
[58] G.-Z. Wang, M.-C. Fu, B. Zhao, R. Shang, *Sci. China: Chem.* **2021**, *64*, 439–444.
[59] M.-C. Fu, J.-X. Wang, R. Shang, *Org. Lett.* **2020**, *22*, 8572–8577.
[60] E. J. McClain, T. M. Monos, M. Mori, J. W. Beatty, C. R. J. Stephenson, *ACS Catal.* **2020**, *10*, 12636–12641.
[61] A. Hossain, A. Bhattacharyya, O. Reiser, *Science* **2019**, *364*, eaav9713.
[62] W.-M. Cheng, R. Shang, *ACS Catal.* **2020**, *10*, 9170–9196.
[63] J. Douglas, M. J. Sevrin, Corey, *Org. Process Res. Dev.* **2016**, *20*, 1134–1147.
[64] P. Li, J. A. Terrett, J. R. Zbieg, *ACS Med. Chem. Lett.* **2020**, *11*, 2120–2130.
[65] H. Kisch, *Adv. Photochem.* **2001**, 93–143.
[66] Y. Uozumi, A. E. Putra, *Synfacts* **2018**, *14*, 0650–0650.
[67] C.-H. Lim, M. Kudisch, B. Liu, G. M. Miyake, *J. Am. Chem. Soc.* **2018**, *140*, 7667–7673.
[68] H. M. Yadav, S. V. Otari, V. B. Koli, S. S. Mali, C. K. Hong, S. H. Pawar, S. D. Delekar, *J. Photochem. Photobiol., A chem.* **2014**, *280*, 32–38.
[69] W. Lisowski, A. Mikolajczyk, B. Bajorowicz, A. Zaleska-Medynska, *Appl. Catal. B-environmental* **2018**, *233*, 301–317.
[70] B. Choudhury, M. Dey, A. Choudhury, *Appl. Nanosci.* **2013**, *4*, 499–506.
[71] X.-Z. Ding, X.-H. Liu, *J. Mater. Res.* **1998**, *13*, 2556–2559.
[72] H. Hou, X. Zhang, D.-S. Huang, X. Ding, S. Wang, X. Yang, S. Li, H. Chen, H. Chen, *Appl. Catal., B* **2017**, *203*, 563–571.
[73] T. Bezrodna, G. Puchkovska, V. Shymanovska, J. Baran, H. Ratajczak, *J. Mol. Struct.* **2004**, *700*, 175–181.
[74] M. Lazzeri, A. Vittadini, A. Selloni, *Phys. Rev. B* **2001**, 63.
[75] T. S. Plett, W. Cai, M. Le Thai, I. V. Vlassiouk, R. M. Penner, Z. S. Siwy, *J. Phys. Chem. C.* **2017**, *121*, 6170–6176.
[76] X. Fan, J. Fan, X. Hu, L. Kang, C. Tang, Y. Ma, H. Wu, Y. Li, *Ceram. Int.* **2014**, *40*, 15907–15917.
[77] X. Jiang, Y. Zhang, J. Jiang, Y. Rong, Y. Wang, Y. Wu, C. Pan, *J. Phys. Chem. C* **2012**, *116*, 22619–22624.
[78] Z. Li, J.-D. Xiao, H.-L. Jiang, *ACS Catal.* **2016**, *6*, 5359–5365.
[79] B. Moss, K. K. Lim, A. Beltram, S. Moniz, J. Tang, P. Fornasiero, P. Barnes, J. Durrant, A. Kafizas, *Sci. Rep.* **2017**, *7*, 2938.
[80] M. Janczarek, E. Kowalska, *Catalysts* **2017**, *7*, 317.
[81] D. O. Scanlon, C. W. Dunnill, J. Buckeridge, S. A. Shevlin, A. J. Logsdail, S. M. Woodley, C. R. A. Catlow, M. J. Powell, R. G. Palgrave, I. P. Parkin, G. W. Watson, T. W. Keal, P. Sherwood, A. Walsh, A. A. Sokol, *Nat. Mater.* **2013**, *12*, 798–801.
[82] P. Deák, B. Aradi, T. Frauenheim, *J. Phys. Chem. C.* **2011**, *115*, 3443–3446.
[83] M. Rafsanjani Dehghazi, Y. Absalan, M. Gholizadeh, M. R. Razavi, K. Souri, *ACS Appl. Nano Mater.* **2023**, *6*, 1106–1118.
[84] J. Khamrai, I. Ghosh, A. Savateev, M. Antonietti, B. König, *ACS Catal.* **2020**, *10*, 3526–3532.
[85] X. Tang, J. Zhang, L. Liu, D. Yang, H. Wang, F. He, *J. Phys. Chem. A, Chem.* **2017**, *337*, 71–81.
[86] Z. Zuo, D. T. Ahneman, L. Chu, J. A. Terrett, A. G. Doyle, D. W. C. MacMillan, *Science* **2014**, *345*, 437–440.
[87] H. Yao, B. Xie, X. Zhong, S. Jin, S. Lin, Z. Yan, *Org. Biomol. Chem.* **2020**, *18*, 3263–3268.
[88] M. Gupta, S. Paul, R. Gupta, *Chin. J. Catal.* **2014**, *35*, 444–450.
[89] P. Rana, N. Singh, P. Majumdar, S. P. Singh, *Coord. Chem. Rev.* **2022**, *470*, 214698.
[90] K. Bhansali, S. Raut, S. Barange, P. Bhagat, *New J. Chem.* **2020**, *44*, 19690–19712.
[91] S. U. Raut, K. R. Balinge, K. J. Bhansali, S. A. Deshmukh, P. R. Bhagat, *Catal. Lett.* **2022**, *153*, 1896–1915.
[92] S. U. Raut, K. R. Balinge, S. A. Deshmukh, S. H. Barange, B. C. Mataghare, P. R. Bhagat, *Catal. Sci. Technol.* **2022**, *12*, 5917–5931.
[93] H. Alinezhad, Z. Tollabian, *Bull. Korean Chem. Soc.* **2010**, *31*, 1927–1930.
[94] H. Alinezhad, M. Tajbakhsh, R. E. Ahangar, *Monatsh. Chem.* **2007**, *139*, 21–25.
[95] A. Nagarsenkar, S. Kumar Prajapti, B. N. Babu, *J. Chem. Sci.* **2015**, *127*, 711–716.
[96] M. Homaee, H. Hamadi, V. Nobakht, M. Javaherian, B. Salahshournia, *Polyhedron* **2019**, *165*, 152–161.
[97] X. Dai, X. Cui, Y. Deng, F. Shi, *RSC Adv.* **2015**, *5*, 43589–43593.
[98] T. Shamim, V. Kumar, S. Paul, *Synth. Commun.* **2013**, *44*, 620–632.
[99] H. A. Patel, M. Rawat, A. L. Patel, A. V. Bedekar, *Appl. Organomet. Chem.* **2019**, *33*, e4767.
[100] S. A. Yakukhnov, V. P. Ananikov, *Adv. Synth. Catal.* **2019**, *361*, 4781–4789.
[101] A. R. Bayguzina, C. F. Musina, R. I. Khusnutdinov, *Russ. J. Org. Chem.* **2018**, *54*, 1652–1659.
[102] W. Hu, Y. Zhang, H. Zhu, D. Ye, D. Wang, *Green Chem.* **2019**, *21*, 5345–5351.
[103] B. Li, Y. Li, J. Zheng, W. Zeng, L. Chen, *Synthesis* **2016**, *49*, 1349–135.

Manuscript received: August 20, 2024